



Cerium oxide nanoparticles at the nano-bio interface: size-dependent cellular uptake

Sushant Singh^{a,b}, Anh Ly^{c,d}, Soumen Das^{a,e}, Tamil S. Sakthivel^{a,b}, Swetha Barkam^{a,f} and Sudipta Seal^{a,b,c,g}

^aNanoscience Technology Center, University of Central Florida, Orlando, FL, USA; ^bAdvanced Materials Processing and Analysis Center, University of Central Florida, Orlando, FL, USA; ^cDepartment of Materials Science and Engineering, University of Central Florida, Orlando, FL, USA; ^dSchool of Mathematical and Physical Sciences, University of Technology Sydney, Ultimo, Australia; ^eAviana Molecular Therapeutic, Orlando, FL, USA; ^fMicron Technology, Boise, ID, USA; ^gCollege of Medicine, University of Central Florida, Orlando, FL, USA

ABSTRACT

Abstract

The authors investigated the role of different size and morphology of cerium oxide nanoparticles (CNPs) in cellular uptake and internalization at the nano-bio interface. Atomic force microscopy (AFM) has been utilized to record changes in the membrane elasticity as a function of ceria particle morphology and concentration. Young's Modulus was estimated in presence and absence of CNPs of different sizes by gauging the membrane elasticity of CCL30 (squamous cell carcinoma) cells. Significant change in Young's Modulus was observed for CNP treatments at higher concentrations, while minimum membrane disruption was observed at lower concentrations. Studies using blocking agents specific to energy-dependent cellular internalization pathways indicated passive cellular uptake for smaller CNPs (3–5 nm). Other observations showed that larger CNPs were unable to permeate the cell membrane, which indicates an active uptake mechanism by the cell membrane. The ability of smaller CNPs (3–5 nm) to permeate the cell membrane without energy consumption by uptake pathways suggests potential for use as nanovectors for the delivery of bioactive molecules. Specifically, the passive uptake mechanism allows for the delivery of surface-bound molecules directly to the cytoplasm, avoiding the extreme chemical conditions of endosomal pathways.

ARTICLE HISTORY

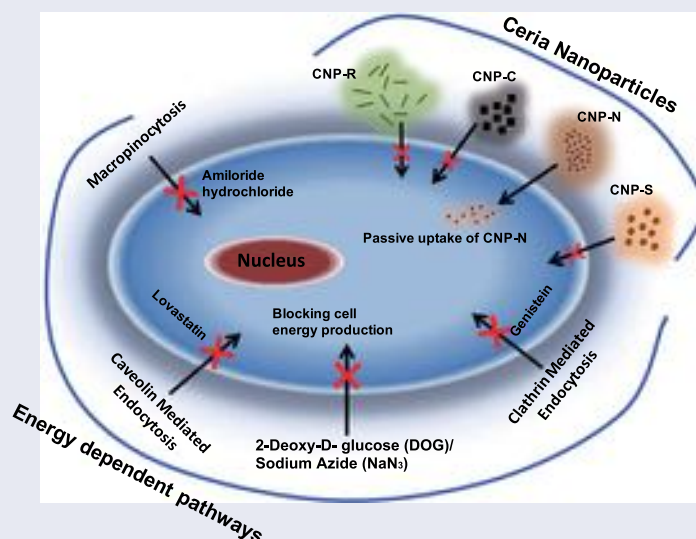
Received 3 August 2018

Revised 29 August 2018

Accepted 30 August 2018

KEYWORDS

Cerium oxide nanoparticle; cellular internalization; membrane elasticity; Young's modulus; passive diffusion; endocytosis



Introduction

Nanomaterials are extensively researched for various applications such as drug delivery, biological sensors, diagnostics and therapeutic imaging [1,2]. Knowledge of the interaction and incorporation of certain nanomaterials into the cellular system creates a new horizon for functional material design research.

The unique physical and chemical properties exhibited by nanomaterials, with respect to their bulk forms, produce unique interactions with biological systems. Characterization of nanomaterial-cell interactions is further complicated by differences in these interactions arising from variation in particle size, structure and composition. Therefore, it is imperative to

understand the interactions of nanomaterials and their effect in the biological environment [3,4].

Experimentally, the interactions between nanomaterials, of a given material composition, and cell membranes can be interpreted as differences in nanomaterial size, surface charge, and agglomeration tendency in biological fluids [5]. These associated physiochemical properties strongly modulate the cellular uptake efficiency of different nanoparticles. Once the nanoparticle is incorporated into a cellular environment, it interacts with a plethora of biomolecules including lipids, proteins and linked carbohydrate molecules found in biological fluids and the cellular plasma membrane [6].

Nanoparticles can cross the cellular membrane through a number of unique endocytotic mechanisms (e.g. macropinocytosis, clathrin-mediated endocytosis, caveolae-mediated endocytosis or a clathrin/caveolae-independent endocytotic mechanism) [7]. Uptake of nanoparticles can also take place by a passive cellular mechanism [8,9]. Reports indicate that small, positively-charged nanoparticles are able to bypass the cellular membrane. However, in these instances, the cell membrane ruptures and a consequent cytotoxic effect is observed [10,11]. Larger nanoparticles have also been found to induce membrane rupture and deformation effects [12].

Cerium oxide nanoparticles (CNPs) have gained a tremendous amount of attention recently due to their highly antioxidative nature and therapeutic potential as nanomedicine in cancer biology [13,14] and neuroprotection [15,16]. As reported earlier, cerium ions can exist in two different oxidation states (Ce^{+3} and Ce^{+4}) [17] due to the production/annihilation of oxygen vacancies in the ceria lattice. Due to the existence of dual oxidation states, CNPs act as “catalytic hotspots” by undergoing redox reactions [18,19]. This mixed valance state of Ce^{+3} and Ce^{+4} helps in scavenging various reactive oxygen species (ROS) and reactive nitrogen species (RNS). *In vivo* and *in vitro* studies have also found CNPs to be highly effective against oxidative stress and chronic inflammation [20,21]. With these properties, CNPs have emerged as effective and fascinating material for bio-nanotechnology applications including biotherapeutics and drug delivery approaches [22,23].

Due to their potential application as a therapeutic agent, CNPs were used as a model system for this study. Here, cellular interaction at the nano-bio interface is characterized with a focus on the energy-dependent and energy-independent uptake mechanisms of different-sized CNPs into the cellular system by analysing the elasticity of the cell membrane.

Materials and methods

Materials

Cerium nitrate hexahydrate (99.999% purity; Cat. No-202991), 30% hydrogen peroxide (Cat. No. H3410), 3-(4,5-Dimethylthiazol-2-yl)-2,5-diphenyltetrazolium bromide (MTT; Cat. No. M5655), 2-deoxy-D-glucose (DOG; Cat. No. D8375), sodium azide (NaN_3) (Cat. No. S2002), trypsin/EDTA (Cat. No. 59430C), poly-D-lysine (PDL) (Cat. No. P6407), 5-(N,N-dimethyl) amiloride hydrochloride (Cat. No. A4562), genistein (Cat. No. G6649) and lovastatin (Cat. No. 438185) were purchased from Sigma-

Aldrich (St. Louis, MO). Inductively coupled plasma standard grade cerium was also purchased from Sigma-Aldrich. Human squamous cell carcinoma (RPMI, 2650; ATCC CCL 30) were purchased from ATCC (Manassas, VA).

Synthesis of cerium oxide nanoparticle

Different sizes of CNPs were synthesized using $\text{Ce}(\text{NO}_3)_3 \cdot 6\text{H}_2\text{O}$ as the source. Small-sized CNPs-N in the size range of 3–5 nm was synthesized using the wet chemical method as described [24]. Preparation of CNPs in different shapes (nanosphere (CNP-S), nanocubes (CNP-C) and nanorods (CNP-R) was performed using a single-step hydrothermal process where $\text{Ce}(\text{NO}_3)_3 \cdot 6\text{H}_2\text{O}$ in the concentration of 0.45–0.6 M were mixed in deionized water and prepared [25].

Instruments and characterization

Characterization of CNPs for size was performed using high-resolution transmission electron microscopy (HRTEM; Philips Tecnai operating at 300 kV). The distribution of size for all the CNPs produced was measured using dynamic light scattering (DLS). The optical and electronic properties of these samples were characterized using UV/visible spectrophotometer (PerkinElmer Lambda 7505, Waltham, MA). The emission properties were measured by exciting the ceria samples at 370 nm. The hydrodynamic radius was estimated using a zeta sizer (Nano-ZS from Malvern Instruments, Malvern, UK) both in PBS and in cell culture media respectively. All CNPs were analysed for hydrodynamic size range upon mixing it with cell culture Eagle's Minimum Essential Medium (EMEM), containing 10% fetal bovine serum (FBS) with 1% antibiotics.

Cell culture experiments

Cell culture analysis with the synthesized CNPs was performed using human squamous carcinoma cells (RPMI 2650; ATCC CCL-30) as a model. Cells were maintained using EMEM containing 10% FBS with 1% antibiotics. Cells were grown up to 90% confluency and were removed from culture flasks with 0.25% trypsin/EDTA solution. Toxicity of different CNPs was studied using the routine MTT assay protocol mentioned earlier [26]. Thiazolyl blue tetrazolium bromide (MTT) was added in the 96-well plate and absorbance was recorded in comparison to the control samples.

Catalytic activity measurement

Catalytic activity measurement of the different CNPs samples for superoxide dismutase (SOD) and catalase (CAT) was also performed. The quantitative determination for SOD and CAT was carried out using SOD assay kit (Sigma Aldrich, Kit #19160-1KTF) and Amplex Red hydrogen peroxide assay kit (Invitrogen, Cat. No. # A22188, Carlsbad, CA) as per instructions provided both in PBS and cell culture media. The CNPs solution was diluted to 1 mM using PBS and cell culture media and the assay was carried out.

Force-distance measurement

Force-distance measurement was carried out using an AFM instrument from Solver Scanning Probe Microscope 2006, obtained from NT-MDT (Moscow, Russia). The measurements were conducted in AFM force-distance mode. A coverslip containing the cells was mounted on a substrate inside the AFM chamber. A cell was selected using an optical microscope, which is connected with the screen. The motion of the AFM tip was recorded as well as the applied force when tapping to the cell. In our experiment, MLCT AFM tip purchased from Bruker (Billerica, MA) was selected for the force-curve measurement. With spring constant from 0.07 to 0.14 N/m, the Bruker microlever AFM probe has a soft silicon nitride cantilever, and the tip is ideal for contact imaging modes, force modulation microscopy and liquid operation. The range in force constant enables users to probe extremely soft samples in contact/tapping mode as well as high load versus distance spectroscopy.

ICP-MS measurement and cellular uptake investigation

Cellular uptake of the amount of CNPs was measured using inductively-coupled plasma mass spectrometry (ICP-MS) as

described [27]. In detail, after the specific incubation time period with CNPs, the cells were washed thrice with PBS, trypsinized, centrifuged and washed thrice more with PBS, leading to removal and separation of any adsorbed CNPs from the cellular surface. Towards determining the amount of cellular uptake of CNPs, the residual cells were digested with 70% nitric acid for 48 h and then diluted to 3.5% nitric acid concentration and was syringe filtered prior to ICPMS measurement. ICPMS grade standard cerium element was used for calibration and CNPs metal concentration measurement was carried out using Varian 820-MS (Axial Simultaneous ICP-MS, New York, NY).

CNPs cellular uptake mechanism was studied using different pharmacological inhibitors for endocytosis pathways. Inhibitors include 5-(N,N-Dimethyl) amiloride hydrochloride, genistein and lovastatin were used with prior treatment with DOG and sodium azide (NaN_3) to inhibit the cellular energy production. The cells were incubated in EMEM serum-free medium for 1 h prior to uptake treatment. CNP was introduced to the cells, incubated for appropriate time, and washed with phosphate buffered saline (PBS) before the force curve measurement.

Results

Physiochemical characterization of CNPs

Uniform-sized CNP nanoparticles of 3–5 nm (CNP-N) were obtained using the wet chemical synthesis method (Figure 1(a)). CNP nanospheres (CNP-S), nanocubes (CNP-C) and nanorods (CNP-R) were prepared through a single step procedure of hydrothermal synthesis, as described in our earlier publication (Figure 1(b–d)) [25]. Particle sizes were determined through HRTEM (Figure 1(b–d)). All CNPs were analysed for hydrodynamic size (*via* DLS) and zeta potential upon mixing with cell culture EMEM, containing 10% FBS with 1% antibiotics (refer Table 1). CNP-N was found to have hydrodynamic radii of 18 nm and zeta potential value of -6.08 mV upon interaction with cell culture growth media. Similarly, CNP-C, CNP-S and CNP-R were found to have higher hydrodynamic radii of 194, 370, and 192 nm with the zeta potential values of -10.86 , -9.98 and -5.9 mV, respectively.

Biocatalytic activity including SOD and CAT mimetic activity of these CNPs was also measured (Figure 2(a,b)). SOD scavenging activity of CNP-N (3–5 nm) was high, compared to that of CNP-S, CNP-C and CNP-R. Cell toxicity analysis of these CNPs was also performed using CCL-30 cell culture model. At 125 μM , all preparations of CNPs were found to be non-toxic to the CCL-30 cell line (Figure 2(c)). Effect of PBS

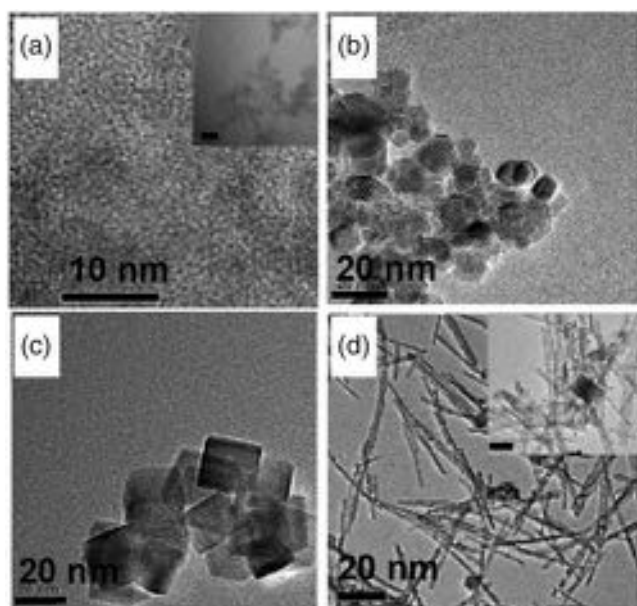


Figure 1. High-resolution transmission electron microscope (HR-TEM) image data of (a) cerium oxide nanoparticles (CNP-N) with diameter 3–5 nm which is prepared by a wet chemical methodology (Scale bar for insert image is 50 nm). The other samples including (b) CNP nanospheres (CNP-S) with diameter 20–30 nm; (c) CNP nanocubes (CNP-C) (d) CNP nanorods (CNP-R) were prepared by hydrothermal process of synthesis (Scale bar for insert image is 100 nm).

Table 1. Comparison between the size and surface zeta potential of different CNPs as measuring in PBS and in cell culture growth media at 250 μM concentration and 60 min of incubation period.

Sample	Size in PBS (nm)	Surface zeta potential in PBS (mV)	Size in cell culture medium (nm)	Surface zeta potential in cell culture medium (mV)
Nanoparticles (CNP-N)	3–5	10.8 ± 1.3	18 ± 2	-6.08 ± 0.21
Nanospheres (CNP-S)	15–20	-21.9 ± 0.43	194 ± 10	-10.86 ± 0.57
Nanocubes (CNP-C)	30	3.95 ± 0.19	370 ± 3	-9.98 ± 1.48
Nanorods (CNP-R)	50–200	-5.11 ± 0.28	192 ± 4	-5.9 ± 0.47

The size analysis was performed using the DLS methodology.

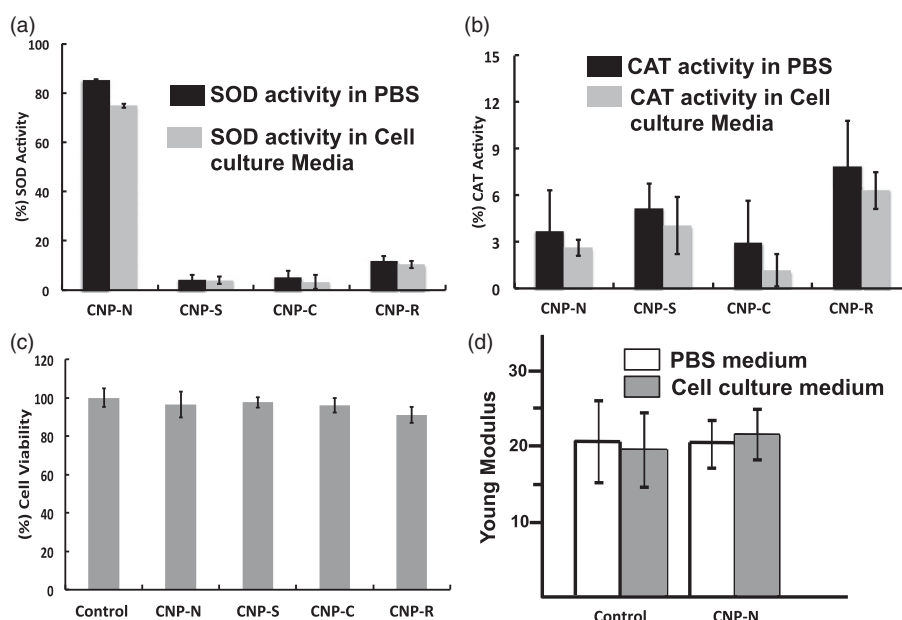


Figure 2. Superoxide dismutase and catalase assay are the antioxidative assay used to determine its reactive oxygen species scavenging potential of the different cerium oxide nanomaterial. (a) Superoxide dismutase (SOD) activity of different CNPs at a concentration of 1 μ M. (b) Catalase (CAT) mimetic properties of different CNPs at similar concentration. Effect of different size of CNPs on the Cell viability of CCL30 cell line was also determined. (c) MTT based cell viability of CCL30 cell lines upon treatment with different size based CNPs at 150 μ M concentration. To identify the effect of media environment, elasticity was determined in phosphate buffer saline (PBS) and cell culture media (EMEM media) (d) Cells Young's modulus of different size based CNPs in PBS vs. cell culture growth medium environment after adding 50 μ M CNPs following by 60 min incubation time period. All the experiments were performed individually in triplicate sets. Data are presented as the mean value of triplicate experiment \pm standard deviation (SD).

on cellular elasticity of CCL-30 cells was additionally tested by Force-Distance Spectroscopy. Figure 2(d) shows the result of measurement where untreated control and 50 μ M CNP-N treated cells for 60 min of incubation in both PBS and cell culture medium. No Significant difference in cell moduli was observed with or without CNP treatment in culture medium or PBS.

Analysing cell membrane elasticity when treated with different CNP

Cell Young Moduli were measured at varied CNP concentrations and incubation time periods (Figure 3). It was observed that adding CNPs of different sizes at 50 μ M did not alter the cell membrane elasticity, initially (Figure 3(c–f)). Specifically, the Young's Modulus of cells was measured to be \sim 20 kPa, which is similar to the control cells without CNP treatment. In the case of 125 μ M CNPs, we found that for 15 min of incubation, there is no effect on membrane elasticity. However, after 30 min of incubation, the membrane elasticity decreases to 15 kPa. At higher CNPs concentration (250 μ M), the cell membrane elasticity drops significantly with increasing incubation time. At this high concentration, we observed significant decrease in cells elasticity from 20 to 5 kPa within 15 min of incubation with CNP-C and CNP-R. Similarly, cell membrane elasticity was found to decrease significantly after treatment with CNP-S (20 nm) after 30 min of incubation. In contrast to these results, smaller sized CNP-N (3–5 nm) was found to decrease the cell membrane elasticity at a much smaller, constant rate than other particle morphologies inducing minimum cellular deformations.

Cellular uptake of CNPs and characterization of uptake mode

ICP-MS analysis was performed to determine the amount of CNPs internalized by CCL30 cells (Figure 4). The data indicates a low concentration of CNP-N (3–5 nm) was internalized at up to 60 min of incubation (Figure 4(a)), relative the other CNP formulations ("at 250 μ M"; 100-fold difference with respect to CNP-S and CNP-R) (Figure 4(b–d)).

To identify the route for cellular internalization, cell cultures were pre-incubated with pathway-specific chemical inhibitors to internalization and subsequently treated with different CNP formulations. To study energy-dependent internalization pathways, 2-DOG and NaN₃ were used to inhibit cellular energy production. The obtained result (Figure 5(a)) indicates that cells incubated with smaller size CNP-N (3–5 nm) exhibited a change in cell membrane elasticity, while the larger nanoparticle CNP-S (20 nm diameter) did not. In another experiment, pre-incubation with lovastatin (an HMG-CoA reductase antagonist; inhibitor of caveolae-mediated endocytosis) and treatment with CNPs did not induce any significant change in cell elasticity. In contrast, when clathrin-mediated endocytosis and macroendocytosis pathways were inhibited by genistein, Young's Modulus changes significantly, indicating CNP cellular internalization.

Discussion

In this study, we characterized the membrane permeation behaviour of different CNP formulations with varying size and morphology. Specifically, flux across a cellular membrane (CCL30, squamous cell carcinoma line) and the mode of

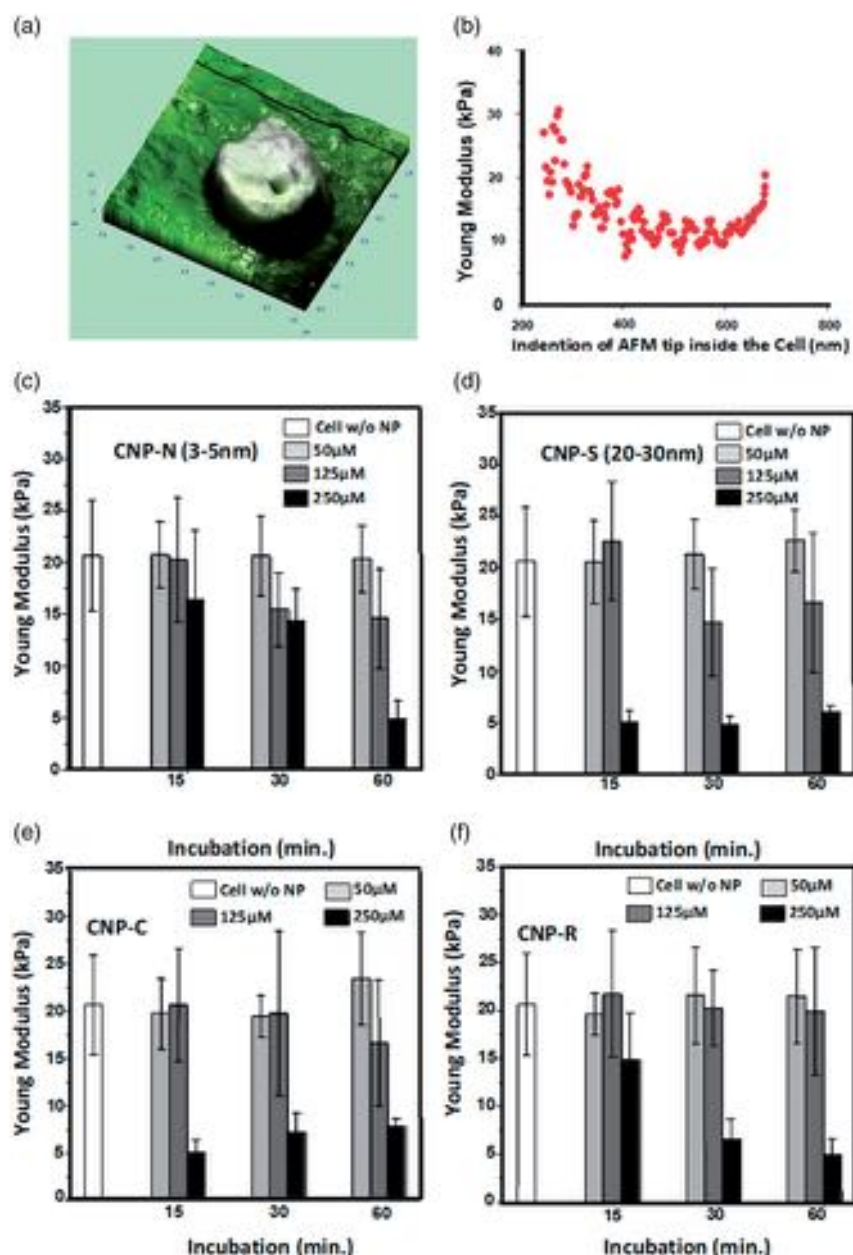


Figure 3. Cells Young's modulus measurement for the different size based CNPs treatment. (a) Cell indentation image as scanned by AFM, (b) Cells Young's modulus vs. the indentation of AFM tip inside. (c) CNPs (3–5 nm) nanoparticle, CNP-N cells Young's modulus vs. incubation time at different CNPs concentration and time period of incubation. (d) CNPs (20–30 nm) nanospheres, CNP-S cell Young's modulus data. (e) CNP-C nanocubes cells Young's Modulus data and (f) CNP-R nanorods cells Young's Modulus data derived after treating with different concentration and time period of incubation. The CNPs concentration employed for cells Young's Modulus measurement were 50, 125 and 250 μM concentration and the time period of incubation were 15, 30 and 60 min for the data analysis. All the experiments were performed individually in triplicates and the data is presented as the mean value of triplicate experiment \pm standard deviation (SD).

pathway action (active or passive) has been analysed, with respect to particle size and morphology.

It is well-established that particle size, surface character, and morphology will influence interactions with bio-structures/systems. However, particles with unique physicochemical properties are needed for varied biomedical applications. Necessarily, these materials will possess widely varying size, surface character and morphology. Thus, the specific influence of these properties needs definition. Nanoparticles prepared by the wet chemical method, a process well-established by our group, leads to the synthesis of small size CNPs in range of 3–5 nm (HRTEM, Figure 1). Different size and morphology nanoparticles, including CNP-nanospheres (20–30 nm; CNP-S), nanocubes (CNP-C), and nanorods (CNP-R), prepared by

hydrothermal method, are represented in HRTEM image, respectively (Figure 1(b–d)). DLS in cell culture media allows characterization of particle aggregation/solution stability, as well as the particles' exclusion volume due to solvent orientation around the particle (as hydrodynamic radius). Our results indicate the formation of a large hydration sphere around particles from each formulation with change in the zeta potential respectively. This characterization is essential for membrane permeation studies, given that the hydration sphere will increase the effective size of the particles and the cellular endocytosis also depends upon the size and surface zeta potential of the nanoparticle (i.e. we can consider the particle radius plus the radius of the hydration sphere as the total size of material being passed through the cell

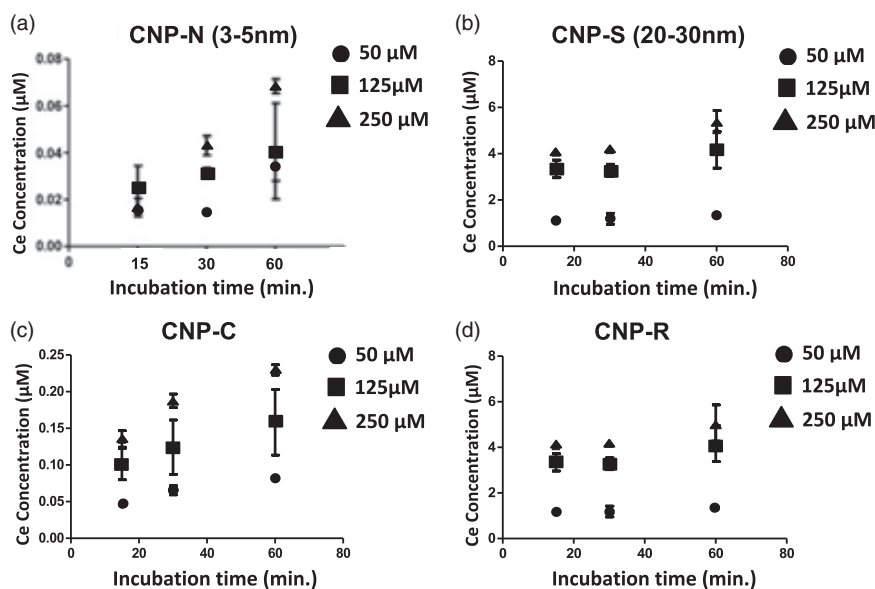


Figure 4. ICP-MS analyses were also performed for measuring the concentration of different sizes of CNPs internalized by the CCL-30 cell lines. For this measurement, CCL30 cells were incubated with 50, 125 and 250 μM concentration of different sizes of CNPs, and the time period of incubation were 15, 30 and 60 min. The ICP-MS analyses were performed on these samples, which are (a) CNP-N, (b) CNP-S, (c) CNP-C and (d) CNP-R. These analyses were performed individually in triplicates and the data are presented as the mean value of triplicate experiment \pm standard deviation (SD).

membrane). Furthermore, these particles were observed as stable following overnight incubation in media. Given these data points, we determined that these particles are best suited for this study. We next sought to determine the catalytic activities for each formulation to highlight their specific potential therapeutic values.

We have shown that CNPs are catalytically active and can scavenge ROS in both *in vitro* and *in vivo* biological systems [28,29]. SOD- and CAT-mimetic activity for all formulations were tested and observed to correlate with $\text{Ce}^{+3}/\text{Ce}^{+4}$ ratio, in accordance with our previously published data. Specifically, it was shown that a higher extent of Ce^{+3} on the surface of synthesized nanoparticles promotes the scavenging of superoxide anions [29]. CAT mimetic assay (scavenging of hydrogen peroxide) showed that CNP-S and CNP-R have higher CAT mimetic activity in comparison to CNP-N and CNP-C, in correlation with their higher relative degrees of Ce^{+4} [26,28]. The enzyme mimetic activity of CNPs was also measured upon mixing with cell culture media and was found to be slightly affected. We attribute this small loss in overall enzyme activity as the blocking of redox active surface sites on the CNP surface by media bio-molecules. In application, this effect is often avoided by coating particle surfaces with a polymer which prevents bio-molecule adsorption through steric hinderance or electrostatic repulsion. However, for this study, we chose to leave the particle surfaces bare to prevent the complication of site/facet-specific adsorption or polymer-membrane interactions in our results. The collected data indicate that these CNPs show unique and substantial catalytic activities, suggesting potential for use in biomedical therapies. However, it has been shown in numerous other studies that larger particles can mediate a toxic cellular response, counter-indicating their use in medicine. Therefore, here, CNPs were tested for general cell toxicity.

All CNP preparations showed no significant toxicity towards CCL30 (cell viability >90%) (Figure 2(c)). Therefore, we

determine that the particles chosen for this study are viable for future biomedical application and, relevant for this study. Additionally, since the particles did not show significant toxicity, they should not induce any apoptosis-related changes to particle membrane elasticity. Thus, we studied the changes in the mechanical properties of CNP-treated cell membrane.

Membrane elasticity is one of the critical features which affects numerous biological processes, including cell growth and differentiation and various cellular uptake processes [30]. Atomic force microscopy (AFM) is a method for obtaining high-resolution images of biological surfaces, including living cells. AFM can be also used to dissect the cell membrane while simultaneously monitoring its mechanical properties (Young's Modulus) [31] at nano-scale resolution. To measure the Young's Modulus (elasticity) of a cell, the AFM probe was brought into incidence with the cell membrane and the cantilever deflection was recorded as a function of the piezoelectric probe's z-position. The force F applied by the sample (cell) on the AFM cantilever was calculated using Hooke's law: $F = k.d$, where $d = \alpha.A$, k is the cantilever's spring constant, A is the measured cantilever's deflection in nA, and α refers to the deflection sensitivity that converts cantilever's deflection from nA to nm. The resulting deflection vs. indentation curve was then fitted using the Hertz model. In order to evaluate the cell's Young's Modulus *via* AFM investigation with the Hertz model, the shape of the probe tip should be taken into account. In our case, the formula for a four-sided pyramid probe is as follows:

$$F = \frac{E}{1 - \nu^2} \frac{\tan \alpha}{\sqrt{2}} \delta^2$$

where

- F : Force acting on the probe
- E : Young's Modulus of the Cell

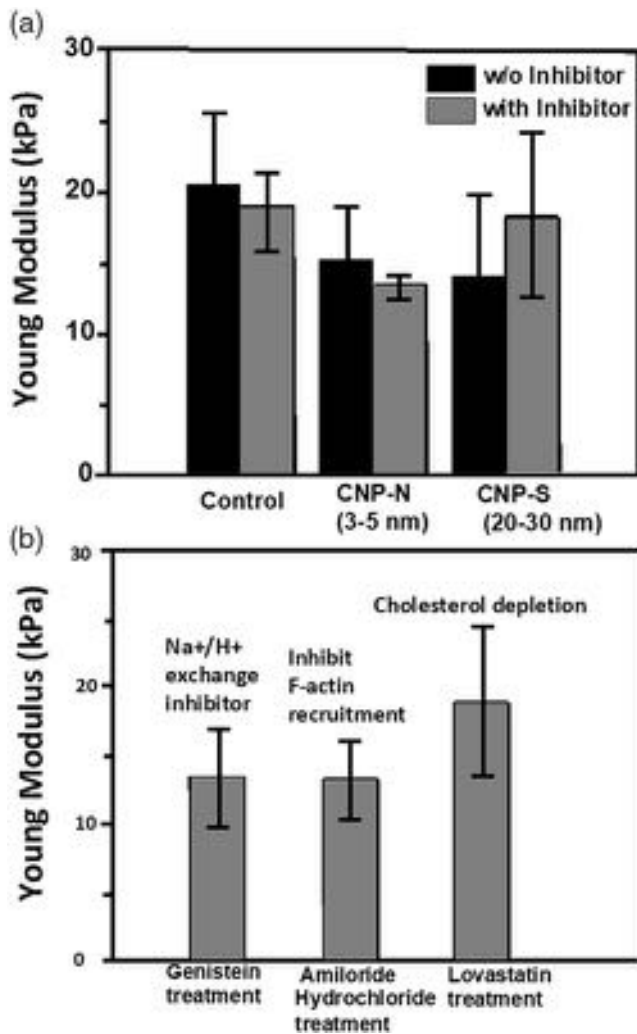


Figure 5. (a) Cells Young's modulus measurement for CNP-N and CNP-S in presence of 2-deoxy-D-glucose (DOG) and sodium azide (NaN_3) inhibitors for cellular energy production. The experiment was carried out at CNPs concentration of $125 \mu\text{M}$ and 60 min of incubation time period. (b) Cells Young's modulus in presence of selective inhibitors which specifically inhibits selective pathway of endocytosis such as amiloride hydrochloride for blocking macropinocytosis pathway, Genistein for blocking the clathrin-mediated endocytosis pathway and lovastatin for blocking the caveolae-mediated endocytosis pathway. The experiment was carried out at CNPs concentration of $125 \mu\text{M}$ and 60 min of incubation time period. These analyses were performed individually in triplicates and the data is presented as the average value of triplicate experiment \pm standard deviation (SD).

- ν : Poisson's ratio
- δ : indentation depth
- α : face angle of the probe

The force curve measurements performed in each of PBS and in cell culture media indicates that cellular elasticity (i.e. Young's Modulus) of the cell remains unaffected in both environments, at 20 kPa. This experiment indicates that PBS is a reasonable surrogate medium for the cellular elasticity measurements in place of cell culture medium, which can produce a more complex signal response due to solution protein interactions with the AFM probe. From here, all elasticity measurements were performed in PBS. The cell's Young's Modulus is dependent on the size and morphology of the CNPs. Analysis indicated that adding different sizes of CNPs at a low concentration of $50 \mu\text{M}$ did not alter the cell membrane elasticity as shown in Figure 3(c–f). This might be due

to the presence of low concentration of CNPs inducing negligible effects onto the cellular membrane for internalization. However, higher CNP concentration and incubation time period lead to significant changes in cellular elasticity. These results indicated that changes in cell elasticity were mediated by nanoparticle-cell interactions as well as the cell internalization process. Observations showed that the internalization of larger size CNPs such as CNP-C and CNP-R was more time consuming, while smaller size nanoparticles internalized much quickly into the cells, causing minimal membrane deformations. Cells treated with smaller CNP-N (3–5 nm) were found to decrease cell membrane elasticity much slower than others, inducing minimum deformations, as shown in Figure 3(c–f). Therefore, small sized CNPs are better for cellular drug delivery, from the standpoint of effect on cellular membrane elasticity and causing minimal cell membrane deformations, as compared to other larger sized CNPs [32].

ICP-MS analysis further supported our understanding of cellular uptake of smaller CNPs. Low concentration of CNP-N was internalized over time while other CNPs were internalized in much higher concentration, as shown in Figure 4(a–d). We hypothesize that the low uptake of CNP-N (3–5 nm) is due to the energy independent internalization passive pathway, where the cellular membrane is not actively involved. Selective entry can also occur through the energy-based active internalization pathway [33]. Depending upon the mechanism of cellular internalization process, the external substances upon interaction may create different impacts to the biological functions of the cellular system. In the energy-independent or passive pathway, cellular membranes uptake the extracellular materials without any consumption of energy. In contrast, the energy-dependent/endocytosis pathway has been the main mechanism for cellular internalization processes. Endocytosis refers to the mechanism of cellular internalization of macromolecules and solutes through cellular membrane bound vesicles engulfed by plasma membrane. Endocytosis is subdivided into two main categories: phagocytosis (i.e. cell eating, where the membrane engulfs large extracellular particles) and pinocytosis, or cell drinking, where the uptake of fluids and solutes takes place. The pinocytic pathway is further divided into three morphologically distinct sub-pathways: Clathrin-mediated endocytosis, Caveolae-mediated endocytosis and Macropinocytosis [34].

In order to identify the route of CNPs cellular internalization, the energy-dependent pathways were inhibited using 2-DOG and NaN_3 treatment. CNP-N (3–5 nm) were found to induce changes in the cell membrane elasticity even when energy-dependent pathways were blocked, while no changes were observed for other CNPs under similar conditions (Figure 5(a)). This confirms that smaller CNP-N (3–5 nm) get internalized through energy independent pathways. In contrast, through using the potential specific energy pathways inhibitor, it was found that CNP-S (20–30 nm) gets internalized using the energy-dependent pathways. Small size nanoparticle (CNP-N, 3–5 nm) gets internalized by passive cellular internalization and avoids the direct engulfment into the lysosome, and can be an ideal delivery vehicle for variety of therapeutic molecules, including RNA and others sensitive drugs [35].

This work is the first reported study where different morphology of CNPs has been examined for cellular uptake and energy dependent or independent cellular internalization. The obtained results indicate the dependence of particle concentration and incubation time period on membrane elasticity and cellular internalization. Low concentration of CNPs at shorter incubation time period did not affect the membrane elasticity, while at higher concentration there was significant change in cellular membrane elasticity, correlating with the nanoparticle cellular internalization. Through application of cellular energy inhibitors, it was shown that smaller CNP-N (3–5 nm) could permeate the cell membrane through energy-independent pathways while under similar conditions, larger formulations (CNP-S, CNP-C and CNP-R) were unable to permeate the cell membrane. Specifically, our results suggest that these particles are taken up through energy-dependent caveolae-mediated pathways. These results lead to a better understanding of the influence of physiochemical properties of CNPs on bio-membranes and their interactions with the biological system. Overall, these findings will input additional guidelines to the design and synthesis of more advanced, biocompatible, and efficient nanomaterials for medicinal and drug delivery approaches.

Acknowledgements

The authors gratefully acknowledge the support of Material Characterization Facility (MCF) provided by the Advanced Materials Processing and Analysis Center and Material Science and Engineering Department for the characterization of different material employed in this manuscript.

Disclosure statement

The authors declare that there is no conflict of interest regarding the publication of this article.

References

- [1] Kim T, Hyeon T. Applications of inorganic nanoparticles as therapeutic agents. *Nanotechnology*. 2014;25:012001.
- [2] Kotov NA, Winter JO, Clements IP, et al. Nanomaterials for neural interfaces. *Adv Mater*. 2009;21:3970–4004.
- [3] Schulte PA, Geraci CL, Murashov V, et al. Occupational safety and health criteria for responsible development of nanotechnology. *J Nanopart Res*. 2014;16:2153.
- [4] Stark WJ. Nanoparticles in biological systems. *Angew Chem Int Ed Engl*. 2011;50:1242–1258.
- [5] Patil S, Sandberg A, Heckert E, et al. Protein adsorption and cellular uptake of cerium oxide nanoparticles as a function of zeta potential. *Biomaterials*. 2007;28:4600–4607.
- [6] Treuel L, Nienhaus GU. Toward a molecular understanding of nanoparticle–protein interactions. *Biophys Rev*. 2012;4:137–147.
- [7] AshaRani PV, Low Kah Mun G, Hande MP, et al. Cytotoxicity and genotoxicity of silver nanoparticles in human cells. *ACS Nano*. 2009;3:279–290.
- [8] Wang T, Bai J, Jiang X, et al. Cellular uptake of nanoparticles by membrane penetration: a study combining confocal microscopy with FTIR spectroelectrochemistry. *ACS Nano*. 2012;6:1251–1259.
- [9] Chithrani BD, Ghazani AA, Chan WC. Determining the size and shape dependence of gold nanoparticle uptake into mammalian cells. *Nano Lett*. 2006;6:662–668.
- [10] Leroueil PR, Berry SA, Duthie K, et al. Wide varieties of cationic nanoparticles induce defects in supported lipid bilayers. *Nano Lett*. 2008;8:420–424.
- [11] Kostarelos K, Lacerda L, Pastorin G, et al. Cellular uptake of functionalized carbon nanotubes is independent of functional group and cell type. *Nature Nanotech*. 2007;2:108–113.
- [12] Zhao Y, Sun X, Zhang G, et al. Interaction of mesoporous silica nanoparticles with human red blood cell membranes: size and surface effects. *ACS Nano*. 2011;5:1366–1375.
- [13] Sack M, Alili L, Karaman E, et al. Combination of conventional chemotherapeutics with redox-active cerium oxide nanoparticles—a novel aspect in cancer therapy. *Mol Cancer Ther*. 2014;13:1740–1749.
- [14] Sack-Zschauer M, Karaman-Aplak E, Wyrich C, et al. Efficacy of different compositions of cerium oxide nanoparticles in tumor-stroma interaction. 2017;13(12):1735–1746.
- [15] Eitan E, Hutchison ER, Greig NH, et al. Combination therapy with lenalidomide and nanoceria ameliorates CNS autoimmunity. *Exp Neurol*. 2015;273:151–160.
- [16] Dowding JM, Song W, Bossy K, et al. Cerium oxide nanoparticles protect against Abeta-induced mitochondrial fragmentation and neuronal cell death. *Cell Death Differ*. 2014;21:1622–1632.
- [17] Xu C, Qu X. Cerium oxide nanoparticle: a remarkably versatile rare earth nanomaterial for biological applications. *NPG Asia Mater*. 2014;6:e90.
- [18] Deshpande S, Patil S, Kuchibhatla SV, et al. Size dependency variation in lattice parameter and valency states in nanocrystalline cerium oxide. *Appl Phys Lett*. 2005;87:133113.
- [19] Kumar A, Babu S, Karakoti AS, et al. Luminescence properties of europium-doped cerium oxide nanoparticles: role of vacancy and oxidation states. *Langmuir*. 2009;25:10998–11007.
- [20] Korsvik C, Patil S, Seal S, et al. Superoxide dismutase mimetic properties exhibited by vacancy engineered ceria nanoparticles. *Chem Commun*. 2007;10(10):1056–1058.
- [21] Dowding JM, Dosani T, Kumar A, et al. Cerium oxide nanoparticles scavenge nitric oxide radical (NO). *Chem Commun*. 2012;48:4896–4898.
- [22] Celardo I, Pedersen JZ, Traversa E, et al. Pharmacological potential of cerium oxide nanoparticles. *Nanoscale*. 2011;3:1411–1420.
- [23] Xu C, Lin Y, Wang J, et al. Nanoceria-triggered synergetic drug release based on CeO₂-capped mesoporous silica host-guest interactions and switchable enzymatic activity and cellular effects of CeO₂. *Adv Health Mater*. 2013;2:1591–1599.
- [24] Das S, Singh S, Dowding JM, et al. The induction of angiogenesis by cerium oxide nanoparticles through the modulation of oxygen in intracellular environments. *Biomaterials*. 2012;33:7746–7755.
- [25] Sakthivel T, Das S, Kumar A, et al. Morphological phase diagram of biocatalytically active ceria nanostructures as a function of processing variables and their properties. *ChemPlusChem*. 2013;78:1446–1455.
- [26] Dowding JM, Das S, Kumar A, et al. Cellular interaction and toxicity depend on physicochemical properties and surface modification of redox-active nanomaterials. *ACS Nano*. 2013;7:4855–4868.
- [27] Hirst SM, Karakoti A, Singh S, et al. Bio-distribution and in vivo antioxidant effects of cerium oxide nanoparticles in mice. *Environ Toxicol*. 2013;28:107–118.
- [28] Pirmohamed T, Dowding JM, Singh S, et al. Nanoceria exhibit redox state-dependent catalase mimetic activity. *Chem Commun*. 2010;46:2736–2738.
- [29] Heckert EG, Karakoti AS, Seal S, et al. The role of cerium redox state in the SOD mimetic activity of nanoceria. *Biomaterials*. 2008;29:2705–2709.
- [30] Discher DE, Janmey P, Wang YL. Tissue cells feel and respond to the stiffness of their substrate. *Science*. 2005;310:1139–1143.
- [31] Allison DP, Mortensen NP, Sullivan CJ, et al. Atomic force microscopy of biological samples. *Wires Nanomed Nanobiotechnol*. 2010;2:618–634.
- [32] Singh R, Lillard JW Jr., Nanoparticle-based targeted drug delivery. *Exp Mol Pathol*. 2009;86:215–223.
- [33] Singh Sushant BN. Membrane biophysics. In: Misra G, editor. *Introduction to biomolecular structure and biophysics*. Singapore: Springer. 2017. p. 183–204.
- [34] GM C. *The cell a molecular approach*. 2nd ed. Sunderland (MA): Sinauer Associates; 2000.
- [35] Shang L, Nienhaus K, Nienhaus GU. Engineered nanoparticles interacting with cells: size matters. *J Nanobiotechnol*. 2014;12:5.

Use of Cerium Oxide Nanoparticles Conjugated with MicroRNA-146a to Correct the Diabetic Wound Healing Impairment



Carlos Zgheib, PhD, Sarah A Hilton, MD, Lindel C Dewberry, MD, Maggie M Hodges, MD, Subhadip Ghatak, PhD, Junwang Xu, PhD, **Sushant Singh, PhD**, Sashwati Roy, PhD, Chandan K Sen, PhD, Sudipta Seal, PhD, Kenneth W Liechty, MD, FACS, FAAP

-
- BACKGROUND:** Diabetic wounds have become one of the most challenging public health issues of the 21st century, yet there is no effective treatment available. We have previously shown that the diabetic wound healing impairment is associated with increased inflammation and decreased expression of the regulatory microRNA miR-146a. We have conjugated miR-146a to cerium oxide nanoparticles (CNP-miR146a) to target reactive oxygen species (ROS) and inflammation. This study aimed to evaluate the consequences of CNP-miR146a treatment of diabetic wounds.
- STUDY DESIGN:** Eight-millimeter wounds were created on the dorsal skin of Db/Db mice and treated with PBS or differing concentrations of CNP-miR146a (1; 10; 100; or 1,000 ng) at the time of wounding. Rate of wound closure was measured until the wounds were fully healed. At 4 weeks post-healing, a dumbbell-shaped skin sample was collected, with the healed wound in the center, and an Instron 5942 testing unit was used to measure the maximum load and modulus.
- RESULTS:** Our data showed that diabetic wounds treated with PBS or 1 ng CNP-miR146a took 18 days to heal. Treatment with 10, 100, or 1,000 ng of CNP+miR-146a effectively enhanced healing, and wounds were fully closed at day 14 post-wounding. The healed skin from the CNP-miR146a-treated group showed a trend of improved biomechanical properties (increased maximum load and modulus), however it did not reach significance.
- CONCLUSIONS:** We found that a 100-ng dose of CNP-miR146a improved diabetic wound healing and did not impair the biomechanical properties of the skin post-healing. This nanotechnology-based therapy is promising, and future studies are warranted to transfer this therapy to clinical application. (J Am Coll Surg 2019;228:107–115. © 2018 by the American College of Surgeons. Published by Elsevier Inc. All rights reserved.)
-

Disclosure Information: Nothing to disclose.

Presented at the American College of Surgeons 104th Annual Clinical Congress, Scientific Forum, Boston, MA, October 2018.

Received July 1, 2018; Revised August 23, 2018; Accepted September 14, 2018.

From the Laboratory for Fetal and Regenerative Biology, Department of Surgery, School of Medicine, University of Colorado Denver - Anschutz Medical Campus and Colorado Children's Hospital, Aurora, CO (Zgheib, Hilton, Dewberry, Hodges, Xu, Liechty); the Department of Surgery, Comprehensive Wound Center, Ohio State University Medical Center, Columbus, OH (Ghatak, Roy, Sen); and the Advanced Materials Processing and Analysis Centre, Nanoscience Technology Center (NSTC), Materials Science and Engineering, College of Medicine, University of Central Florida, Orlando, FL (Singh, Seal).

Correspondence address: Kenneth W Liechty, MD, FACS, FAAP, University of Colorado Denver — Anschutz Medical Campus, 12700 E 19th Ave, RC2 Bldg, 6th Floor, Aurora, CO 80045. email: Kenneth.Liechty@childrenscolorado.org

Diabetes has reached pandemic proportions worldwide. Complications of diabetes, such as impaired wound healing, represent a significant medical problem; the annual cost of diabetic lower extremity ulcers alone ranges from \$9 billion to \$13 billion, in addition to the cost for management of diabetes mellitus alone.^{1,2} In addition, an ulcer of the lower extremity precedes 85% of all diabetic lower extremity amputations, and is the primary cause for hospitalization among diabetics.³ Despite the enormous impact of these wounds on both individuals and society, effective therapies are lacking. Therefore, the modification or correction of diabetic impaired wound healing has far-reaching consequences, both on patient outcomes and on health care expenditures.

Normal wound repair follows an orderly and well-defined sequence of events that requires the interaction

Abbreviations and Acronyms

CNP	= cerium oxide nanoparticles
Db	= diabetic
IL-6	= interleukin-6
IL-8	= interleukin-8
miR-146a	= microRNA-146a
NFkB	= nuclear factor kappa B
ROS	= reactive oxygen species
STZ	= streptozocin

of many cell types and growth factors, and it is divided into inflammatory, proliferative, and remodeling phases.⁴ In diabetic wounds, this complex orchestration of wound healing processes and phases are disrupted. Although the etiology is multifactorial, increased and persistent inflammation and increased oxidative stress have been implicated as central features of the wound healing impairment and complications in people with diabetes.⁵⁻¹⁰

The diabetic wound healing impairment and ulcer formation starts with a predisposed susceptibility for injury at baseline. We have previously shown that unwounded murine diabetic skin is biomechanically inferior when compared with skin on nondiabetic controls.¹¹ We found that murine diabetic skin had a much lower maximum stress and a decreased modulus of elasticity. We also showed that the biomechanical properties of diabetic skin decline during the progression of the diabetic phenotype, which increases the susceptibility of diabetic skin to injury.⁹ On the other hand, we found that at 4 weeks after wounding, healed murine diabetic wounds showed no significant difference in biomechanical properties when compared with nondiabetic wounds.¹¹ Diabetic maximum stress and modulus were similar to those in nondiabetic samples.

Small RNA molecules or microRNA (miRNA) have been demonstrated to regulate the protein production of proinflammatory cytokines at the post-transcription level.^{12,13} In particular, miR-146a has been described as one of the key regulatory molecules in the inflammatory response, acting as a “molecular brake” on the inflammatory response. MiR-146a targets and represses interleukin-1 receptor-associated kinase 1 (IRAK1) and tumor necrosis factor receptor-associated factor 6 (TRAF6). These 2 key adapter molecules of the NFkB pathway increase NFkB activity, resulting in increased expression of the genes interleukin (IL)-6 and IL-8.¹⁴⁻¹⁸ We recently showed that diabetic wounds have decreased expression of miR-146a during the wound healing response.¹⁸ We demonstrated that decreased miR-146a resulted in increased gene expression of its target genes,

interleukin-1 receptor-associated kinase 1 and tumor necrosis factor receptor-associated factor 6, and a subsequent increase in NFkB signaling. Decreased expression of miR-146a in diabetic wounds may be responsible for the increased gene expression of the pro-inflammatory cytokines IL-6 and IL-8/MIP-2 and the increased inflammation seen in diabetic wounds.

Some diseases, including diabetes, have been linked to accumulation of reactive oxygen species (ROS) and their undesired effects, such as the activation of redox-sensitive transcription factors, especially NFkB.^{19,20} This resulted in increased expression and production of proinflammatory cytokines such as IL-6 and IL-8, which are key mediators of inflammation. Recently, nonviral miRNA delivery strategies using nanoparticles demonstrated success. One particular type of nanoparticles present several advantages as an appropriate vehicle to deliver therapeutic miRNAs to a diabetic wound site. Cerium oxide nanoparticles (CNP) possess auto-regenerative, radical-scavenging properties due to the nanocrystalline structure of cerium oxide and the valence structure of the cerium atom caused by coexistence of 2 oxidation states reversibly switchable between 3+ and 4+ in the presence of ROS.²¹⁻²³ By scavenging the excess of ROS, these nanoparticles may be able to eliminate oxidative stress and correct the imbalance between oxidants and antioxidative enzymes in diabetic wounds.

Therefore, we propose that delivery of the anti-inflammatory miR-146a via conjugation with the antioxidative stress CNP (CNP-miR146a) decreases inflammation and oxidative stress, which will result in correction of impaired healing and improved biomechanical properties of the healed skin.

METHODS**Diabetic mouse model**

All experimental protocols were approved by the Institutional Animal Care and Use Committee at University of Colorado Denver - Anschutz Medical Campus and followed the guidelines described in the NIH Guide for the Care and Use of Laboratory Animals. For all experiments, 12-week-old female mice homozygous for the *Leprdb* mutation (db/db) were used (BKS.Cg-Dock7m+/+*Leprdb*/J, strain No. 000642, Jackson Laboratory).

Cerium oxide nanoparticles synthesis and characterization

The CNP nanoparticles were synthesized using simple wet chemistry methods, as described previously.²⁴ In a

typical synthesis, a stoichiometric amount of cerium nitrate hexahydrate (99.999% from Sigma-Aldrich) was added to 50 mL of deionized water (18.2 MV) and stirred for 1 hour. The cerium (III) ions in the solution were oxidized to cerium (IV) oxide using excess hydrogen peroxide. After that, the pH of the solution was kept below 3.5 1 N nitric acid to maintain the synthesized ceria nanoparticles in suspension. Crystalline nanoparticles of cerium oxide form immediately on oxidation. Nanoparticles were isolated by centrifugation at 8,000 *g* for 10 minutes. Ten μM of nanoceria was prepared from 5 mM of nanoceria suspension by small aliquot dilution in pure water. Hydrodynamic size and zeta potential measurements were carried out at varying pH using dynamic light scattering measurements from Zeta Sizer Nano (Malvern Instruments), which uses a laser with wavelength at 633 nm. Different pH values in the suspension were adjusted using either ammonium hydroxide or nitric acid.

Murine wound healing model and treatment

Mice were anesthetized with inhaled isoflurane. Each mouse was shaved and depilated before wounding. The dorsal skin was swabbed with alcohol and Betadine (Purdue Pharma). Each mouse underwent a single dorsal full-thickness wound (including panniculus carnosus) with an 8-mm punch biopsy (Milrex Inc). These wounds were treated with 50 μL of PBS, 100 ng of CNP alone, 10^6 pfu of lent-miR146a, or differing concentrations of CNP-miR146a (1; 10; 100; or 1,000 ng) at the time of wounding (Fig. 1A). All wounds were dressed with Tegaderm (3M), which was subsequently removed on postoperative day 2. Postoperatively, the mice received a subcutaneous injection of an analgesic, buprenorphine (Schering-Plough Animal Health Corp).

Murine wound area measurement

Photographs were obtained with a Nikon camera (Nikon) using a ruler for each image. ImageJ software (National Institutes of Health; <http://rsbweb.nih.gov/ij/>) was used to calculate the wound area of each mouse every other day. A blinded observer analyzed the size of each wound. Wound area was plotted as a function of time.

Biomechanical testing of murine skin

Biomechanical testing was performed on a full-thickness skin area from the treated mice, including the wounded area. Biomechanical testing was done 28 days post-healing on wounded skin treated with PBS or CNP-miR146a (1; 10; 100; or 1,000 ng). Skin samples immediately underwent testing after harvest; all samples had their subcutaneous tissue removed, and a uniform, dumbbell-shaped testing unit was stamped out using

well-established, previously described techniques.^{9,11} Cranial-caudal orientation was preserved. Two Verhoeff stain lines were placed on either end of the dumbbell shape, demarcating the gauge length of the testing area. The mean cross-sectional area of the samples tested was calculated as precisely as possible to ensure that an accurate modulus and maximum stress were calculated. The ends of the testing unit were fixed between sandpaper using a cyanoacrylate adhesive to prevent slipping. The testing unit was mounted in custom designed fixtures and tested in tension using an Instron 5543 test frame (Instron). Each testing unit underwent a previously established protocol. In short, the testing unit was preloaded to 0.005 Newtons (N), held for 120 seconds, and then subjected to a constant increase in force until the sample failed (as evidenced by tearing of the skin) and was no longer able to hold tension. Maximum stress to failure was calculated using linear regression from the linear region of the stress-strain curve. The modulus of elasticity was calculated as the slope of the stress-strain curve within the elastic region of the ramp to failure.

Swine excisional wound model and treatment

A Yorkshire white male pig was used in this study. All procedures were approved by the Ohio State University Institutional Laboratory Animal Care and Use Committee (ILACUC). To induce diabetes, the pig was injected with streptozocin (STZ) (75 mg/kg body weight) only once. To avoid hypoglycemia due to insulin released by the destroyed beta cells, 200 mL of a 5% glucose solution were given over a period of 1 hour after STZ application. Four weeks after STZ injection, the pig (47 kg) was sedated by Telazol (Butler Schein) and anesthetized by mask with isoflurane (3% to 4%). The dorsal region was shaved. The skin was surgically prepared with alternating chlorhexidine 2% and alcohol 70% (Butler Schein) scrubs. Under such aseptic conditions, 2 sets of 5 full-thickness excisional wounds (1"×1") were established on the back of pigs with a depth of approximate 2 cm, to reach the subcutaneous fat in all wounds. A total of 5 wounds were created on each side of the back. A scaled plastic template was used to create the wounds at fixed distance from each other and from the spine (4 cm), starting below the lower border of the scapula on the dorsum of the pig. Wounds from 1 side of the back were treated with a CNP-miR146a (100 ng) followed by dressing with Tegaderm, while the wounds from the contralateral side of the back were dressed with Tegaderm only and received only PBS (control). Digital photographs were taken on days 0, 3, 7, 10, and 14 for measurement of the wound area. The pig was maintained on 12-hour light–dark cycles and was euthanized 14 days post-wounding.

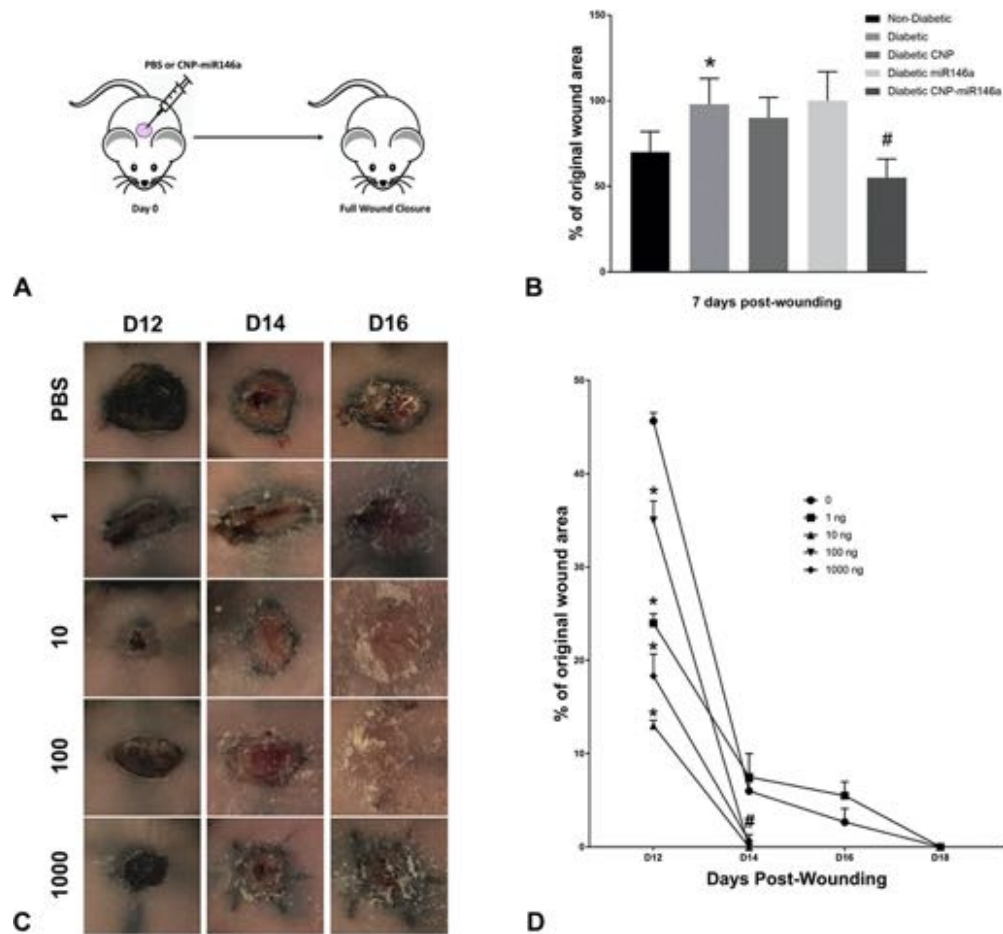


Figure 1. Cerium oxide nanoparticles (CNP)-miR146a improve diabetic wound healing. (A) Graphic representation of the wounding protocol and treatment in the diabetic mouse. (B) Graphic representation of nondiabetic wounds (PBS), diabetic wounds (PBS), and diabetic wounds treated with 100 ng CNP, 10^6 PFU LentimiR-146a, or 100 ng of CNP-miR146a at day 7 post-wounding. * $p < 0.05$ compared with nondiabetic wounds and # $p < 0.05$ compared with diabetic wounds by Student's *t*-test. (C) Representative photographs (days 12, 14, and 16 post-wounding) of diabetic murine wounds treated with 0 (PBS), 1, 10, 100, or 1,000 ng of CNP-miR146a at the time of wounding. (D) Graphic representation of wound closure timeline in diabetic wounds treated with 0 (PBS), 1, 10, 100, or 1,000 ng of CNP-miR146a at the time of wounding. $n = 3$ per group; * $p < 0.05$ comparing 0 to 1 ng, 0 to 10 ng, 0 to 100 ng, or 0 to 1,000 ng; # $p < 0.05$ comparing 0 or 1 ng to 10, 100, or 1,000 ng by Student's *t*-test.

All wounds were digitally photographed in the presence of a standard reference ruler. Wound area was calculated using the ImageJ software. The pig was maintained on standard chow ad libitum, fasted overnight before the procedures, and housed individually in the animal facility. The pig was maintained on 12-hour light–dark cycles and was euthanized after the completion of experiments.

Swine wounds histologic analysis

At day 14 post-wounding, the animal was euthanized and the wound-edge tissue (2 cm from the edge) was collected in formalin from the control (PBS) and treated (1,300 ng CNP-miR146a). Five-micron microtomed sections were

placed on positive charged slides. Some slides underwent Masson's Trichrome staining. The rest of the slides were deparaffinized. Once sections were hydrated they were placed in citrate buffer pH 6.0, and heat-induced epitope retrieval was performed using the Biocare Medical's Decloaker. The slides were then stained using Leica's Bond Rx instrument, and all reagents were applied robotically onto slides. The slides were incubated with primary CD45 and CD31 antibodies (BD Biosciences) at 1:50 dilutions. They were developed with a Vectastain Elite ABC kit with secondary antibody (Vector Laboratories). A blinded observer analyzed the numbers of CD31-positive and CD45-positive cells per high-power field.

Statistical analysis

The *t*-test was used to analyze the data. All data were expressed as the mean \pm SEM and a value of $p < 0.05$ was considered significant.

RESULTS

Treatment of diabetic wounds with CNP-miR146a accelerates healing

Figure 1B shows the percentage of original wound area at day 7 post-wounding for nondiabetic wounds (PBS), diabetic wounds (PBS), and diabetic wounds treated with 100 ng CNP, 10^6 PFU LentimiR-146a, or 100 ng of CNP-miR146a. The percentage of open wounds among diabetic wounds is significantly higher than in nondiabetic wounds at day 7 post-wounding. Treatment with 100 ng of CNP-miR146a significantly enhances diabetic wound healing. On the other hand, CNP or miR-146a alone did not improve healing. Treatment of diabetic wounds with the CNP-miR146a resulted in a significant improvement of wound healing. Diabetic wounds treated with PBS (0 ng) were significantly larger at days 14 and 16 compared to diabetic wounds treated with CNP-miR146a (Fig. 1C). Our data showed that diabetic wounds treated with PBS or 1 ng CNP-miR146a took 18 days to heal. Treatment with 10, 100, or 1,000 ng of CNP+miR-146a effectively enhanced the rate of wound closure, and wounds were fully closed at day 14 post-wounding (Fig. 1D).

Diabetic skin maintained its biomechanical properties post-healing

At 4 weeks after wounding, healed murine diabetic wounds treated with (1, 10, or 100 ng) CNP-miR146a showed a trend toward improved biomechanical properties compared with the PBS-treated wounds; however, it did not reach significance (Fig. 2A). The average modulus for the healed skin treated with PBS was 11.09 ± 5.98 MPa (Fig. 2B). For the healed skin treated with 1, 10, 100, and 1,000 ng of CNP-miR146a, the average modulus was 13.5 MPa, 13.71 MPa, 12.6, and 8.5 MPa, respectively (Fig. 2B).

Diabetic skin did not develop any pathologic abnormalities after treatment

Histopathologic microscopic examination of skin samples from mice treated with PBS or different doses of CNP-miR146a did not reveal any pathology or lesions (Fig. 3). In addition, no soft tissue abnormalities were noted in the majority of tissues; multiple soft tissues were microscopically reviewed, there was excess adipose

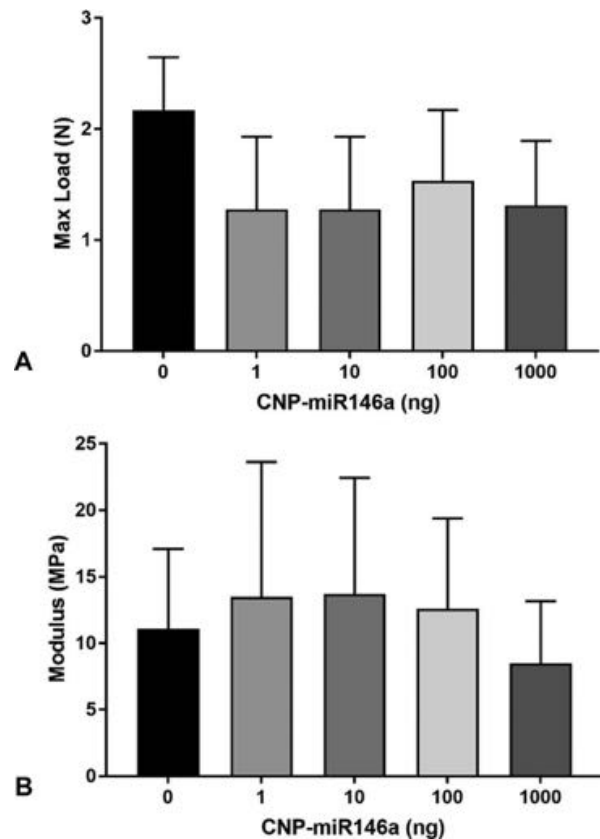


Figure 2. Cerium oxide nanoparticles (CNP)-miR146a maintained the biomechanical properties of diabetic skin post-healing. Figure 2A displays the maximum load and 2B displays the modulus of skin samples collected at day 28 post-healing from wounds treated with 0 (PBS), 1, 10, 100, or 1,000 ng of CNP-miR146a at the time of wounding. Student's *t*-test showed no significant difference between the treatment groups.

tissue, but nothing appeared abnormal for this strain of diabetic mouse.

CNP-miR146a improves healing in a clinically relevant model of diabetes

To induce diabetes, the pig was injected with STZ (75 mg/kg body weight) only once, as shown in Figure 4A. Wounds were created at 1 month post-STZ injection. Five of 10 wounds on the right side were treated with CNP-miR146a at day 0, as shown in Figure 4B. Digital imaging of the wounds was performed on days 0, 3, 7, 10, and 14 for measurement of wound area. Figure 4C shows representative digital photographs of 2 wounds at day 14, 1 treated with PBS and another with CNP-miR146a. These photographs show that at day 14 post-wounding, the wound treated with CNP-miR146a is clearly smaller in size compared with the wound treated with PBS.

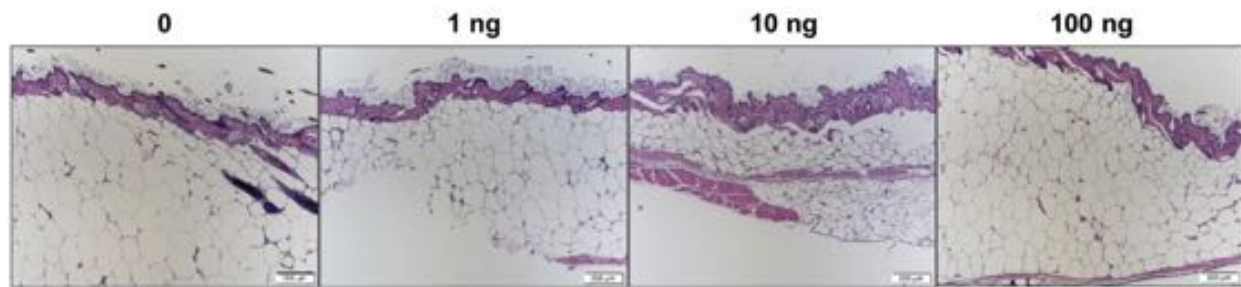


Figure 3. Cerium oxide nanoparticles (CNP)-miR146a did not induce any pathologic abnormalities in the diabetic skin post-healing. Histopathologic microscopic examination of skin samples from diabetic wounds treated with 0 (PBS), 1, 10, 100 ng of CNP-miR146a at day 28 post-healing.

Figure 4D shows graphic analysis of the areas of all 10 wounds, measured by digital planimetry. At day 10, the PBS-treated wounds had an average surface area of $6.8 \text{ cm}^2 \pm 0.46$; the surface area of the CNP-miR146a treated wounds was $4.8 \text{ cm}^2 \pm 0.24$. By day 14, the average surface areas of the PBS and CNP-miR146a treated wounds were $4.63 \text{ cm}^2 \pm 0.21$ and $3.06 \text{ cm}^2 \pm 0.28$, respectively (Data expressed as mean \pm SEM, * $p < 0.05$).

CNP-miR146a decreases inflammation and increases angiogenesis in diabetic wounds

The effect of CNP-miR146a treatment on inflammation was assessed using immunohistochemistry for CD45, the common leukocyte antigen. Representative photos of immunoperoxidase staining for CD45 at 14 days in swine diabetic wounds treated with PBS or CNP-miR146a are demonstrated in Figure 5A. Quantitative analysis of diabetic wounds treated with CNP-miR146a demonstrated a significant decrease in CD45-positive cells compared with PBS-treated diabetic wounds (Fig. 5B).

The effect of CNP-miR146a treatment on angiogenesis was assessed using immunohistochemistry for endothelial marker CD31. Representative photos of immunoperoxidase staining for CD31 at 14 days in swine diabetic wounds treated with PBS or CNP-miR146a are shown in Figure 5A. Quantitative analysis of diabetic wounds treated with CNP-miR146a demonstrated a significant increase in the number of vessels compared with PBS-treated diabetic wounds (Fig. 5B).

The effect of the CNP-miR146a on fibrosis was assessed at 14 days using trichrome staining. Representative sections from both PBS- and CNP-miR146a-treated wounds are displayed in Figure 5. Treatment with CNP-miR146a did not result in a significant change in fibrosis compared with the PBS-treated diabetic wounds.

DISCUSSION

This study demonstrates the potential of a novel therapeutic agent for diabetic wounds, CNP-miR146a. Local treatment of the diabetic wound with CNP or miR146a alone did not have an effect on the rate of wound closure in diabetic wounds; however, treatment with CNP-miR146a conjugate resulted in reduced time to wound healing, with increased strength and elasticity in a murine model (Figs. 1 and 2). This was further validated in a porcine model in which treatment with CNP-miR146a resulted in reduced time to wound healing, with associated decreased inflammation and increased angiogenesis (Figs. 4 and 5). No adverse effects from treatment with CNP-miR146a were seen in the murine or porcine model (Fig. 3). These findings are promising for the clinical application of this nanoparticle therapeutic in the challenging area of diabetic wound healing.

Previous studies have demonstrated the important role of miR-146a in decreasing pathologic inflammation in the diabetic wound and have shown that the treatment of diabetic wounds with mesenchymal stem cells increased miR-146a expression.¹⁸ However, application of mesenchymal stem cells as a therapeutic remains challenging, highlighting the need for a different delivery mechanism, such as conjugated nanoparticles. In another murine wounding model, application of cerium oxide nanoparticles has demonstrated accelerating wound healing through proliferation of fibroblasts, keratinocytes, and vascular endothelial cells.²³ This is likely related to the ROS scavenging properties of cerium oxide nanoparticles as well as modulation of the intracellular oxygen environment.^{25,26} Therefore, combining these properties of cerium oxide nanoparticles with the anti-inflammatory properties of miR-146a, as in our study, results in decreased inflammation, increased angiogenesis, and improved wound healing.

Wound healing progresses through inflammatory, proliferative, and remodeling phases. In diabetic wounds,

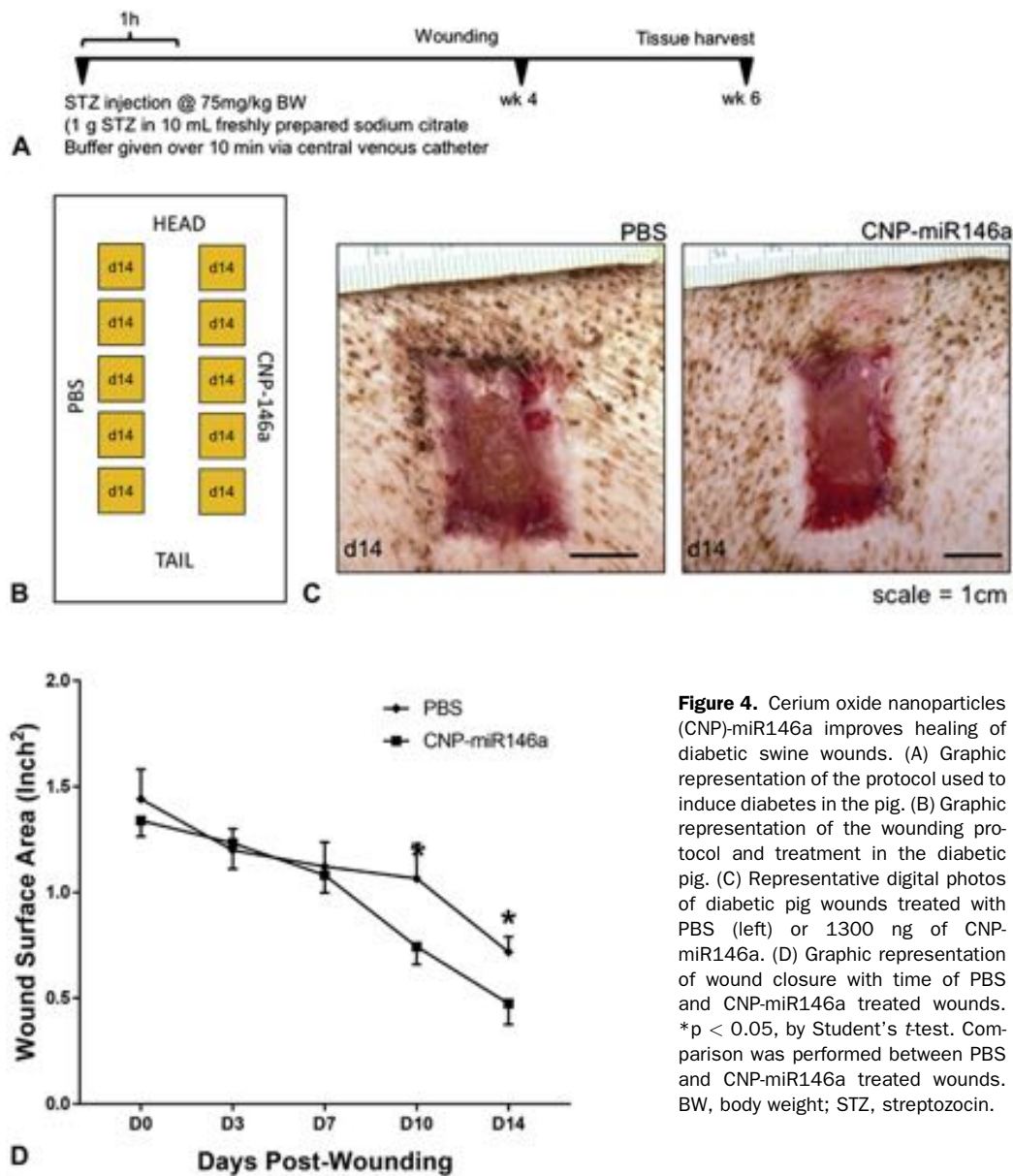


Figure 4. Cerium oxide nanoparticles (CNP)-miR146a improves healing of diabetic swine wounds. (A) Graphic representation of the protocol used to induce diabetes in the pig. (B) Graphic representation of the wounding protocol and treatment in the diabetic pig. (C) Representative digital photos of diabetic pig wounds treated with PBS (left) or 1300 ng of CNP-miR146a. (D) Graphic representation of wound closure with time of PBS and CNP-miR146a treated wounds. * $p < 0.05$, by Student's *t*-test. Comparison was performed between PBS and CNP-miR146a treated wounds. BW, body weight; STZ, streptozocin.

these phases are dysregulated with a prolonged inflammatory phase. Treatment with CNP-miR146a decreases the inflammation in the wound and allows the wound to progress to the proliferative and remodeling phase (Fig. 5). This is supported by our study; the porcine model not only demonstrates a statistically significant improved rate of wound closure in the treatment group, but also, improved granulation tissue and wound appearance of CNP-miR146a group at 14 days (Fig. 4). Furthermore, there is evidence to suggest dysregulation in the

proliferative and remodeling phases as well, with diabetic skin demonstrating decreased collagen I levels and collagen I:III ratios compared with normal skin. This is associated with decreased strength and elasticity on evaluation with biomechanical testing.^{9,11} Our study suggests that this inherent dysregulation of proliferation and remodeling, with resulting decreased strength and elasticity, may be corrected with CNP-miR146a treatment, but further testing is needed. Compared with other therapeutics on the market that decrease time to wound healing,

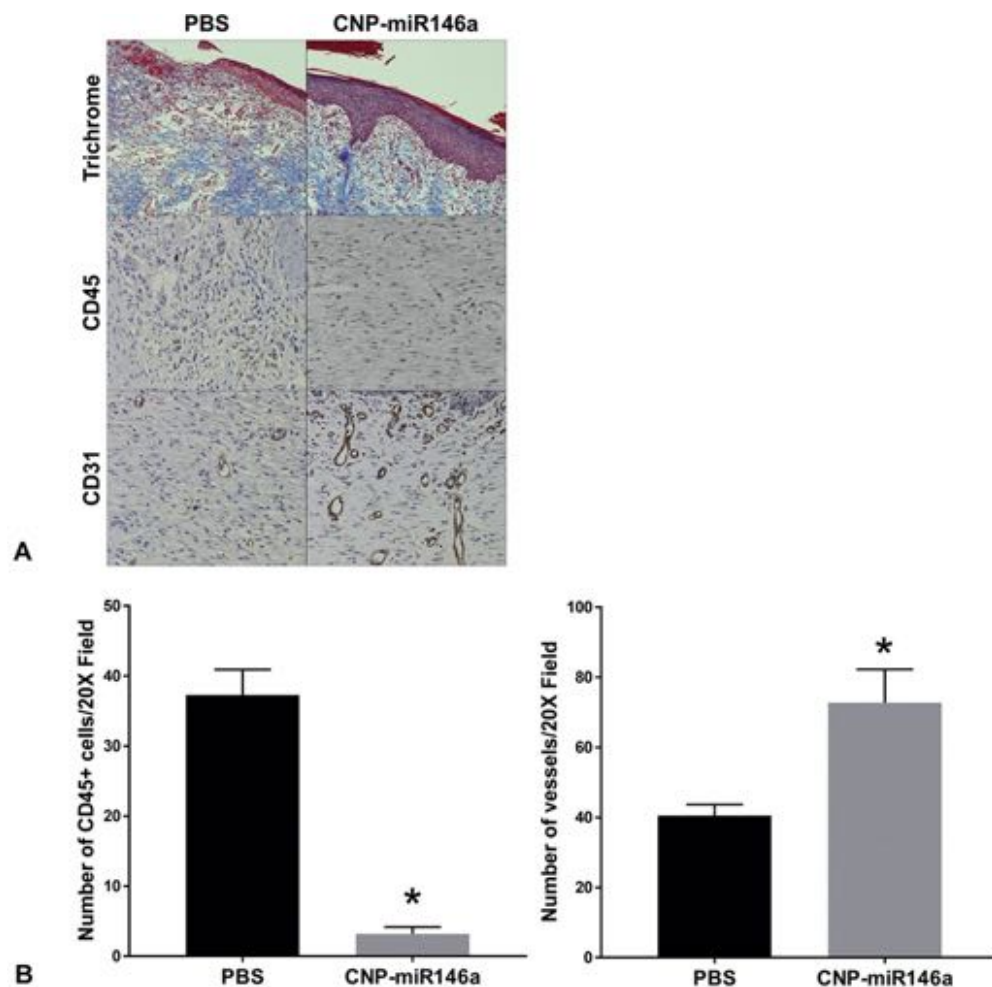


Figure 5. Cerium oxide nanoparticles (CNP)-miR146a-treated wounds showed similar fibrosis levels, decreased inflammation, and increased angiogenesis. (A) Masson's trichrome, CD45+, and CD31+ staining of representative sections of diabetic swine wounds after 14 days of treatment with treated with PBS (n = 5) or CNP-miR146a (n = 5). (B) Quantitative analysis of number of CD45 positive cells and number of vessels (CD31 staining) per 20 \times field. *p < 0.05, by Student's *t*-test. Comparison was performed between PBS and CNP-miR146a treated wounds.

such as platelet-derived growth factor, CNP-MiR146a has the ability to improve both time to wound closure and ultimate skin strength.²⁷

A strength of this study includes the use of a porcine wounding model in addition to a murine model. Porcine skin better represents wound healing seen in humans with regard to granulation tissue and epithelialization, providing a more clinically relevant model than mice. The persistent hyperglycemia induced in pigs leads to delayed epithelialization and impaired wound healing, similar to that in human diabetic wounds.

Diabetic mice are a well-established model for dysfunctional wound healing, but this model is limited due to the contracture that occurs in mice during

healing. Other authors have used devices to prevent wound contracture in mice, but this model still does not account for granulation seen in human wound healing. Therefore, we chose to move further study to the porcine model. Diabetic mice are a well-established model for dysfunctional wound healing, but this model is limited due to the contracture that occurs in mice during healing. Other authors have used devices to prevent wound contracture in mice, but this model still does not account for granulation seen in human wound healing. Therefore, we chose to move further study to the porcine model. The porcine model is limited due to the acute nature of induced diabetes and a lack of long-term diabetic sequela.

CONCLUSIONS

In conclusion, CNP-miR146a improves wound healing in a murine and porcine diabetic wound model without compromising wound strength or elasticity. Future directions include validation in human clinical trials.

Author Contributions

Study conception and design: Zgheib, Hilton, Roy, Sen, Seal, Liechty

Acquisition of data: Zgheib, Hilton, Dewberry, Hodges, Ghatak

Analysis and interpretation of data: Zgheib, Hilton, Dewberry, Hodges, Ghatak, Xu, Singh, Roy, Sen, Seal, Liechty

Drafting of manuscript: Zgheib, Hilton, Dewberry, Hodges, Ghatak, Xu, Singh, Roy, Sen, Seal, Liechty

Critical revision: Zgheib, Hilton, Roy, Sen, Seal, Liechty

Acknowledgment: We would like to thank Professor Linda K Johnson DVM, MS, MPH, Director of the Comparative Pathology Shared Resource (CPSR), Department of Pathology, UC Denver, Anschutz Medical Campus, for her help with the pathology analysis.

REFERENCES

- Ragnarson Tennvall G, Apelqvist J. Health-economic consequences of diabetic foot lesions. *Clin Infect Dis* 2004;39[Suppl 2]:S132–S139.
- Rice JB, Desai U, Cummings AK, et al. Burden of diabetic foot ulcers for Medicare and private insurers. *Diabetes Care* 2014;37:651–658.
- Boulton AJ, Vileikyte L, Ragnarson-Tennvall G, et al. The global burden of diabetic foot disease. *Lancet* 2005;366:1719–1724.
- Lepäntalo M, Apelqvist J, Setacci C, et al. Chapter V: Diabetic foot. *Eur J Vasc Endovasc Surg* 2011;42[Suppl 2]:S60–S74.
- Eming SA, Martin P, Tomic-Canic M. Wound repair and regeneration: mechanisms, signaling, and translation. *Sci Transl Med* 2014;6:265sr6.
- Khanna S, Biswas S, Shang Y, et al. Macrophage dysfunction impairs resolution of inflammation in the wounds of diabetic mice. *PLoS One* 2010;5:e9539.
- Dhall S, Do DC, Garcia M, et al. Generating and reversing chronic wounds in diabetic mice by manipulating wound redox parameters. *J Diabetes Res* 2014;2014:562625.
- Zgheib C, Xu J, Liechty KW. Targeting inflammatory cytokines and extracellular matrix composition to promote wound regeneration. *Adv Wound Care (New Rochelle)* 2014;3:344–355.
- Zgheib C, Hodges M, Hu J, et al. Mechanisms of mesenchymal stem cell correction of the impaired biomechanical properties of diabetic skin: The role of miR-29a. *Wound Repair Regen* 2016;24:237–246.
- Zgheib C, Liechty KW. Shedding light on miR-26a: Another key regulator of angiogenesis in diabetic wound healing. *J Mol Cell Cardiol* 2016;92:203–205.
- Bermudez DM, Herdrich BJ, Xu J, et al. Impaired biomechanical properties of diabetic skin implications in pathogenesis of diabetic wound complications. *Am J Pathol* 2011;178:2215–2223.
- Moura J, Børsheim E, Carvalho E. The role of microRNAs in diabetic complications-special emphasis on wound healing. *Genes (Basel)* 2014;5:926–956.
- Mulholland EJ, Dunne N, McCarthy HO. MicroRNA as therapeutic targets for chronic wound healing. *Molec Ther Nucleic Acids* 2017;8:46–55.
- Xie Y, Chu A, Feng Y, et al. MicroRNA-146a: A comprehensive indicator of inflammation and oxidative stress status induced in the brain of chronic T2DM rats. *Front Pharmacol* 2018;9:478.
- Feng Y, Chen L, Luo Q, et al. Involvement of microRNA-146a in diabetic peripheral neuropathy through the regulation of inflammation. *Drug Des Devel Ther* 2018;12:171–177.
- Lo WY, Peng CT, Wang HJ. MicroRNA-146a-5p mediates high glucose-induced endothelial inflammation via targeting interleukin-1 receptor-associated kinase 1 expression. *Front Physiol* 2017;8:551.
- Bhatt K, Lanting LL, Jia Y, et al. Anti-inflammatory role of microRNA-146a in the pathogenesis of diabetic nephropathy. *J Am Soc Nephrol* 2016;27:2277–2288.
- Xu J, Wu W, Zhang L, et al. The role of microRNA-146a in the pathogenesis of the diabetic wound-healing impairment: correction with mesenchymal stem cell treatment. *Diabetes* 2012;61:2906–2912.
- Wei W, Liu Q, Tan Y, et al. Oxidative stress, diabetes, and diabetic complications. *Hemoglobin* 2009;33:370–377.
- Zgheib C, Hodges MM, Hu J, et al. Long non-coding RNA Lethe regulates hyperglycemia-induced reactive oxygen species production in macrophages. *PLoS One* 2017;12:e0177453.
- Walkey C, Das S, Seal S, et al. Catalytic properties and biomedical applications of cerium oxide nanoparticles. *Environ Sci Nano* 2015;2:33–53.
- Das S, Dowding JM, Klump KE, et al. Cerium oxide nanoparticles: applications and prospects in nanomedicine. *Nanomedicine (Lond)* 2013;8:1483–1508.
- Chigurupati S, Mughal MR, Okun E, et al. Effects of cerium oxide nanoparticles on the growth of keratinocytes, fibroblasts and vascular endothelial cells in cutaneous wound healing. *Biomaterials* 2013;34:2194–2201.
- Karakoti AS, Monteiro-Riviere NA, Aggarwal R, et al. Nanoceria as antioxidant: synthesis and biomedical applications. *JOM (1989)* 2008;60:33–37.
- Korsvik C, Patil S, Seal S, et al. Superoxide dismutase mimetic properties exhibited by vacancy engineered ceria nanoparticles. *Chem Commun (Camb)* 2007;10:1056–1058.
- Das S, Singh S, Dowding JM, et al. The induction of angiogenesis by cerium oxide nanoparticles through the modulation of oxygen in intracellular environments. *Biomaterials* 2012;33:7746–7755.
- Wieman TJ, Smiell JM, Su Y. Efficacy and safety of a topical gel formulation of recombinant human platelet-derived growth factor-BB (becaplermin) in patients with chronic neuropathic diabetic ulcers. A phase III randomized placebo-controlled double-blind study. *Diabetes Care* 1998;21:822–827.